Design and performance of BOREAS, the beamline for resonant X-ray absorption and scattering experiments at the ALBA synchrotron light source

Alessandro Barla,[a,b]* Josep Nicolás,[a] Daniele Cocco,[c]
Secundino Manuel Valvidares,[a] Javier Herrero-Martín,[a] Pierluigi Gargiani,[a]
Jairo Moldes,[a] Claude Ruget,[a] Eric Pellegrin[a] and Salvador Ferrer[a]

[a]ALBA Synchrotron Light Source, E-08290 Cerdanyola del Vallès, Barcelona, Spain, [b]Istituto di Struttura della Materia (ISM), Consiglio Nazionale delle Ricerche (CNR), I-34149 Trieste, Italy, and [c]SLAC National Accelerator Laboratory, 94025 Menlo Park, USA. *Correspondence e-mail: alessandro.barla@trieste.ism.cnr.it

The optical design of the BOREAS beamline operating at the ALBA synchrotron radiation facility is described. BOREAS is dedicated to resonant X-ray absorption and scattering experiments using soft X-rays, in an unusually extended photon energy range from 80 to above 4000 eV, and with full polarization control. Its optical scheme includes a fixed-included-angle, variable-line-spacing grating monochromator and a pair of refocusing mirrors, equipped with benders, in a Kirkpatrick–Baez arrangement. It is equipped with two end-stations, one for X-ray magnetic circular dichroism and the other for resonant magnetic scattering. The commissioning results show that the expected beamline performance is achieved both in terms of energy resolution and of photon flux at the sample position.

1. Introduction

Advanced studies of the magnetic and electronic structure of materials have greatly benefited from the development of a manifold of powerful techniques, based on the resonant absorption or diffraction of X-rays. These include X-ray magnetic circular dichroism (XMCD), X-ray linear dichroism (XLD) and resonant soft X-ray scattering (RSXS) (Stöhr & Siegmann, 2006; Beaurepaire et al., 2013). They combine chemical, orbital and crystal-site selectivity with an extremely high magnetic sensitivity, down to isolated atoms (Carbone et al., 2011). These properties, combined with the high brilliance of third-generation synchrotron sources, have made this set of techniques invaluable for the investigation of ever more complicated magnetic materials and nanometer-sized devices.

Within the recently developed national synchrotron radiation centers in Europe, the ALBA facility (Einfeld, 2011) is currently operating a storage ring with an energy of 3 GeV and at a current of 130 mA. Among the seven operating phase I beamlines, BOREAS (Beamline fOr REsonant Absorption and Scattering experiments) is dedicated to the study of the magnetic properties of materials by means of the techniques based on the dichroism in the absorption or on the resonant diffraction of X-rays. It is equipped with two end-stations: HECTOR (High fiEld veCTOR magnet), dedicated to XMCD/XLD, and MARES (MAgnetic REsonant Scattering end-station), dedicated to RSXS.

BOREAS is based on a grating monochromator and covers a very extended photon energy range, from 80 eV to above
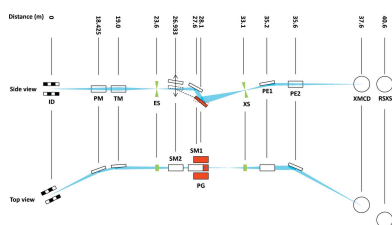
4000 eV, with high flux and energy resolution, together with full control of the polarization state of the X-ray beam. The energy region between 2000 and 4000 eV, where the interesting $L_{2,3}$ absorption edges of the $4d$ transition metals are located, is particularly challenging for XMCD experiments. Indeed, this range is usually covered with Si double-crystal monochromators, because of the low diffraction efficiency of gratings. The degree of circular polarization transmitted by the common Si(111) crystals, however, depends strongly on energy below about 4000 eV. It approaches zero around 2800 eV, where the Bragg angle is equal to the Brewster angle (Rogalev *et al.*, 2016), thus making XMCD experiments impossible or very difficult in the energy range between 2500 and 3200 eV. The grating monochromator of BOREAS, on the other hand, does not alter the polarization state of the X-rays emitted by the beamline undulator, while its reduced diffraction efficiency compared with a crystal monochromator above 2000 eV is compensated by a constant and high degree of circular polarization (this is typically chosen to be 75–85% at BOREAS).

In this article, we describe the principal guidelines upon which the optical layout of the beamline is based, as well as the elements composing the various optical sections, and we discuss the results of the first commissioning phase of the beamline components, giving a detailed account of the photon flux and energy resolution achieved at the sample position.

2. Optical layout design

The optical layout of BOREAS is shown in Fig. 1. This includes a white-beam section with a plane mirror (PM) and a toroidal mirror (TM), a monochromator section with two spherical mirrors (SM1 and SM2), three plane gratings (PG), and an entrance (ES) and an exit slit (XS), and finally a refocusing section with two bendable plane elliptical mirrors (PE1 and PE2). The final design is the result of the balance between several constraints:

(i) The main working energy range should be covered by the beamline with a single set of optical elements. This is identified as the energy interval between 400 and 1600 eV, where the most important absorption edges for studies of magnetism (3d transition-metal L-edges, rare-earth M-edges) as well as of organic/molecular systems (nitrogen and oxygen K-edges) are situated.

(ii) The beamline should reach a minimum energy of 99 eV, where the $L_{2,3}$ absorption edges of Si are located, with circular polarization.

(iii) The single insertion device that can be hosted at the available straight section (section 29 of the ALBA storage ring) should reach the highest photon energy compatible with the above constraint using its first harmonic, in order to maximize its flux with fully circular polarization.

(iv) The photon energy range above 1600 eV should be covered without any degradation of the performance at the lower energies and with the minimum possible number of optical elements.

(v) The beamline monochromator should simultaneously provide a good repeatability of the grating angular motion and a fast scanning speed. This is a consequence of the fact that dichroism experiments typically require the acquisition of several energy scans with different light polarizations, which are subsequently subtracted from each other.

(vi) The refocusing section has to provide variable X-ray beam spot sizes at both end-stations, being located at 3 m distance from one another along the X-ray beam propagation direction.

(vii) The maximum distance between the source and the sample position cannot exceed 41 m.
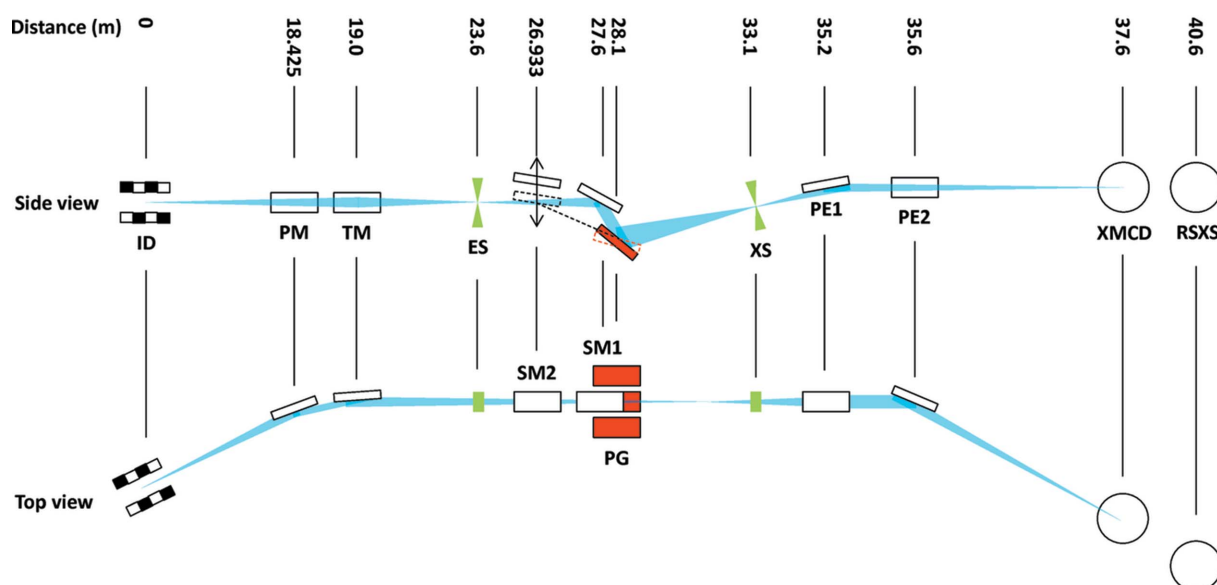

Figure 1
Side and top views of the optical layout of the BOREAS beamline. The depicted optical elements are: ID = Apple-II undulator, PM = plane mirror, TM = toroidal mirror, ES = entrance slit, SM1 = first spherical mirror, SM2 = second spherical mirror, PG = plane gratings, XS = exit slit, PE1 = first plane-elliptical mirror, PE2 = second plane-elliptical mirror. The experimental end-stations are indicated as XMCD and RSXS.

Table 1
Undulator specifications.

Source type		PPM Apple-II
Period	(mm)	71.36
Number of periods		22
Magnetic gap	(mm)	15.5–90.0
Magnetic length	(mm)	1570
Polarization modes		Circular/elliptical/linear (0 to 90°)
Lowest energy (horizontal polarization)	(eV)	59
Lowest energy (circular polarization)	(eV)	78
Lowest energy (vertical polarization)	(eV)	98

Table 2
White-beam section optics specifications.

		PM	TM
Shape		Plane	Toroidal
Position	(m)	18.425	19.0
Source distance (tangential/sagittal)	(m)	–/–	19.0/19.0
Image distance (tangential/sagittal)	(m)	–/–	12.1/4.6
Grazing incidence angle	(°)	1.0	1.15
Geometrical surface size	(mm)	480 × 60	450 × 50
Optical surface size	(mm)	400 × 45	400 × 15
Blank material		Si	Si
Water cooling		Side	Side
Roughness (r.m.s.)†	(nm)	0.13	0.16
Coating material		Au/Ni	Au
Coating thickness	(nm)	50	50
Tangential radius of curvature	(mm)	∞	736652
Sagittal radius of curvature	(mm)	∞	148.65
Tangential slope error (r.m.s.)†	(μrad)	0.75	0.89
Sagittal slope error (r.m.s.)†	(μrad)	3.6	1.83

† Measured value.

The design of the beamline was consequently oriented towards a fixed-included-angle, variable-line-spacing (VLS) grating monochromator of the Hettrick–Underwood type (Hettrick & Underwood, 1986; Underwood & Koch, 1997), equipped with an entrance slit. This allows for simple energy scanning with a single moving element (the grating), while covering a wide photon energy range with a combination of only three plane gratings and two retractable spherical pre-mirrors within the dispersive section. In the following subsections, each optical section and its elements are described in detail.

2.1. Source

The source is a PPM (Pure Permanent Magnet) APPLE-II helical undulator (Sasaki, 1994), inserted in the center of one of the medium straight sections of the ALBA storage ring (Campmany *et al.*, 2013). This type of undulator is capable of delivering linearly polarized light, in all directions within the plane perpendicular to the propagation direction of the photon beam, as well as circularly/elliptically polarized light. The main characteristics of the BOREAS undulator are summarized in Table 1. The minimum magnetic gap of the undulator is limited to 15.5 mm for field homogeneity reasons, while the total magnetic forces are limited to 20 kN. The undulator has 22 periods of 71.36 mm length each, resulting in a total length of 1569.92 mm. This insertion device has been designed in order to allow for reaching the Si $L_{2,3}$-edges (at an energy of 99 eV) with circular polarization at a storage ring energy of 3 GeV, while extending its first emission harmonic to the highest possible energy. With the chosen parameters, the source can be tuned to energies down to 59 eV in linear horizontal polarization, 78 eV in circular polarization and 98 eV in linear vertical polarization. The first harmonic extends up to about 1100 eV, while higher energies are reached by using higher harmonics, trading off the circular polarization rate in favor of the photon flux for higher odd harmonics for experiments requiring circularly polarized light up to 4000 eV.

2.2. White-beam section

The characteristics of the optical elements within the white-beam section are summarized in Table 2. The main function of the first optics section is to isolate the downstream mono-chromator section from thermal drifts by absorbing most of

the power accepted by the beamline. Two mirrors are used to deviate the beam away from the undulator axis, thus simplifying the radiation shielding requirements, and to spread the power density, thus simplifying the required cooling scheme of each mirror. The first optical element of the beamline is a simple plane mirror (PM), which must absorb most of the heat-load without degrading the beam profile. A grazing-incidence angle of only 1° has therefore been chosen in order to stretch the power footprint as much as possible on the surface of the mirror, so as to minimize the power density. PM has two stripes, coated with Au and Ni, in order to maximize its reflectivity across the whole energy range of the beamline. The Au stripe has a higher reflectivity in the energy ranges 80–150 eV, 800–2000 eV and above 3500 eV, while the Ni stripe optimizes the reflectivity of PM in the remaining energy intervals.

The second mirror (TM) has a toroidal profile and focuses the beam vertically onto the entrance slit of the mono-chromator, thus demagnifying the vertical source size by a factor of about four. It also focuses the beam horizontally 2 m upstream of the exit slit of the monochromator. This position for the horizontal focus has been chosen in order to reduce the power density at the exit slit without degrading the energy resolution of the beamline. Due to its strong sagittal curvature, this mirror has a single stripe coated with Au, and a low grazing incidence angle of 1.15° which ensures high reflectivity up to energies of the order of 4000 eV.

2.3. Monochromator

The dispersive section of BOREAS is based on a fixed-included-angle, variable-line-spacing grating monochromator. Although designs based on a variable included-angle offer enhanced flexibility in terms of the tradeoff between energy resolution, photon flux and higher-orders rejection (Follath & Senf, 1997; Follath, 2001), we privileged a design with a simple single moving element (*i.e.* the gratings pitch axis) during fast energy scans. The chosen Hettrick–Underwood design has also fewer optical elements along the dispersive section (just

Table 3
Monochromator optics specifications.

		SM1	SM2	LEG	MEG	HEG
Shape		Spherical	Spherical	Plane	Plane	Plane
Position	(m)	27.6	26.933	28.1	28.1	28.1
Source distance	(m)	4.0	3.333	–	–	–
Image distance	(m)	5.5	6.167	–	–	–
Grazing incidence angle	(°)	1.75	0.75			
Geometrical surface size	(mm)	250×50	250×50	170×25	170×25	170×25
Optical surface size	(mm)	200×15	200×15	150×15	150×15	150×15
Blank material		Si	Si	Si	Si	Si
Water cooling		Side	Side	Side	Side	Side
Roughness (r.m.s.)†	(nm)	0.08	0.15	0.12	0.12	0.13
Coating material		Au	Ni	Ni	Rh	Au
Coating thickness	(nm)	50	50	41†	35†	34†
Radius of curvature	(mm)	151664	330597	∞	∞	∞
Tangential slope error (r.m.s.)†	(µrad)	0.19	0.19	0.21	0.19	0.22
Sagittal slope error (r.m.s.)†	(µrad)	2.48	1.04	0.34	0.29	0.34
Line density (center), D_0	(mm^{-1})	–	–	200	800	1200
Line density, linear variation, D_1	(mm^{-2})	–	–	0.07994	0.31994	0.47997
Line density, quadratic variation, D_2	(mm^{-3})	–	–	0.0000239	0.0000884	0.0001428
Groove profile		–	–	Laminar	Blazed	Blazed
Groove depth†	(nm)	–	–	34.6	–	–
Groove-to-period ratio		–	–	0.775	–	–
Blaze angle†	(°)	–	–	–	0.64	0.55

† Measured value.

mirror and grating), thus maximizing the energy stability and repeatability of the beamline.

The dispersive section includes an entrance slit (ES), two interchangeable spherical mirrors (SM1 and SM2), three interchangeable plane diffraction gratings (LEG, MEG and HEG) and an exit slit (XS). The main characteristics of the optical elements are listed in Table 3. The design has been based on the requirement to achieve a resolving power of at least $E/\Delta E = 5000$ with entrance and exit slits gap not smaller than 15 µm up to an energy of $E = 2000$ eV. This could be achieved with the layout shown in Fig. 1, with the following characteristics:

(i) The distance between ES and XS was fixed to 9.5 m, the maximum allowed by the available floor space.

(ii) A monochromator exit arm (*i.e.* the distance between the grating pole and XS) of 5 m, as a result of the best compromise between the target resolving power and the mechanical requirements (*i.e.* angular resolution and stability of the grating pitch rotation mechanism).

(iii) Two fixed included angles were chosen, as determined by the selected spherical mirror: 175° with SM1 and 177° with SM2.

(iv) SM1 and SM2 are located upstream and as close as possible to the gratings in order to achieve the maximum possible vertical demagnification of the monochromatic beam at XS.

The choice of the variable line spacing ensures the focusing of all the wavelengths diffracted in the first inner diffraction order at almost the same position of the exit slit (*i.e.* at a grating–XS distance which varies by only a few millimeters with varying energy), thus making energy scans possible with a fixed position of the exit slit with negligible degradation of the energy resolution. Moreover, the variable line spacing of the gratings efficiently corrects for their aberrations, so as to

minimize the beam size at the exit slit. The groove density for the VLS gratings is defined as $D(y) = D_0 + D_1 y + D_2 y^2$, where y is the longitudinal coordinate (along the beam propagation direction), D_0 is the groove density in the centre of the grating ($y = 0$), and D_1 and D_2 are the coefficients of the linear and quadratic variation of the groove density along the grating surface. The energy range between 80 and 4500 eV can be covered with only three gratings with different central line spacing D_0: LEG ($D_0 = 200$ lines mm^{-1}) covering the energy ranges 80–300 eV (with SM1) and 250–600 eV (with SM2), MEG ($D_0 = 800$ lines mm^{-1}) for the ranges 380–1700 eV (with SM1) and 950–3000 eV (with SM2), and HEG ($D_0 = 1200$ lines mm^{-1}) in the ranges 600–2100 eV (with SM1) and 1900–4500 eV (with SM2). For each grating, D_1 has been optimized so as to minimize the energy dependence of the longitudinal position of the focal spot at the exit slit.

Fig. 2 shows the diffraction efficiency of all combinations of spherical mirrors and plane gratings of the BOREAS monochromator, in the energy range 80–4500 eV, as calculated using the code *REFLEC* (Schäfers *et al.*, 2002) and with the ALBA ray-tracing code *ART* (Nicolás *et al.*, 2013). The monochromator diffraction efficiency is thus above 15% for energies up to about 2500 eV. This is achieved in the lower energy range of the beamline (up to about 600 eV) with a laminar profile for LEG, that also ensures a good rejection of higher diffraction orders. In order to maximize the grating diffraction efficiency at energies above 1500 eV where MEG and HEG are used in combination with SM2, a blazed groove profile has been chosen with blaze angles of 0.64° and 0.55° for MEG and HEG, respectively. With these blazed profiles, one achieves an efficiency above 5% for energies up to about 4000 eV, while keeping an enhanced higher-order suppression in the photon energy range where MEG and HEG are used in combination with SM1 (*i.e.* 350–1800 eV).
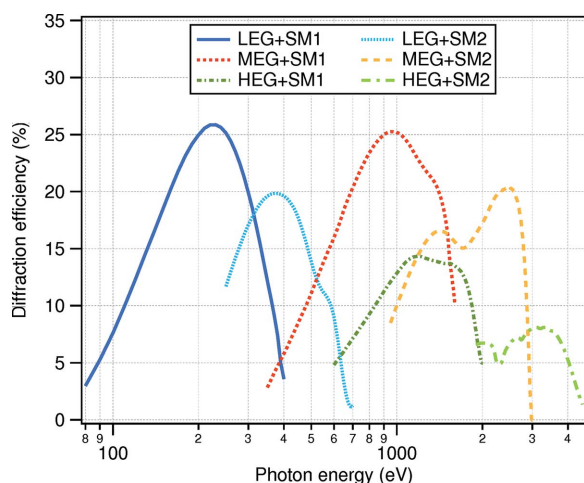
Figure 2
Diffraction efficiency of all available combinations of spherical mirrors and plane gratings.

Table 4
Refocusing section optics specifications.

		PE1	PE2
Shape		Plane elliptical	Plane elliptical
Position	(m)	35.2	35.6
Source distance	(m)	2.1	4.5
Image distance (min/max)	(m)	2.4/∞	2.0/∞
Grazing incidence angle	(°)	0.75	0.75
Geometrical surface size	(mm)	300 × 40	300 × 40
Optical surface size	(mm)	240 × 12	240 × 12
Blank material		Si	Si
Water cooling		–	–
Roughness (r.m.s.)	(nm)	0.5	0.5
Coating material		Au	Au
Coating thickness	(nm)	50	50
Tangential slope error (r.m.s.)†	(μrad)	1.08	1.2
Sagittal slope error (r.m.s.)	(μrad)	5.0	5.0

† Measured on the mirror prior to mounting in its bender.

2.4. Refocusing section

The refocusing section needed to be sufficiently flexible to allow focusing of the X-ray beam at two end-stations located at 3 m distance from one another along the beam propagation direction. Moreover, at each end-station the user needs to be able to tune the beam size to the specific experimental requirements. In some cases (*e.g.* very tiny or inhomogeneous samples) the beam should be reduced to the smallest achievable size, whereas for other applications (*e.g.* very sensitive samples for which a strongly reduced power density is required) a defocused beam is envisaged. For these reasons, a set of two bendable plane-elliptical mirrors (PE1 and PE2) arranged in a Kirkpatrick–Baez geometry (Kirkpatrick & Baez, 1948) have been chosen (see Table 4 for a summary of their specifications).

The maximum distance between XS and the first experimental end-station allowed by the available floor space is fixed at 4.5 m. This impacts the maximum achievable demagnification of the source at the image/sample point. With the choice of placing the horizontally focusing mirror (PE2) downstream of the vertically focusing one (PE1), in order to have a more circular beam profile, the source demagnification is at best about 2 in the horizontal direction and around 1 in the vertical direction. In practice, PE1 focuses the beam vertically in a range tunable between about 30 and 500 μm (40 and 1000 μm) full width at half-maximum (FWHM) at the first (second) end-station, while PE2 focuses the X-rays horizontally to a size between 80 and 500 μm (250 and 1000 μm) FWHM at the first (second) end-station. For a fixed total photon flux, the combined available range of variation of the beam size allows therefore for tuning the X-ray power density at the sample by a factor of more than 100.

3. Operation and performance

3.1. Polarization

3.1.1. Linear polarization. Due to the absence of the on-axis emission of even harmonics, the beamline operates system-atically with odd undulator harmonics when linear polarization is required. The beamline undulator can be controlled in order to change continuously the direction of the polarization vector within an angle of 180° in the plane perpendicular to the X-rays propagation direction. This is particularly advantageous as it allows one to rotate the relative angle between the photon polarization and the sample without any rotation of the latter, which would unavoidably lead to changes in the electron yield and in the sampling depth.

In order to demonstrate this operation mode of the beamline, Fig. 3 shows the XAS spectra recorded at the C K-edge on a highly oriented pyrolitic graphite (HOPG) crystal, at an incidence angle of 30° from the sample surface. The XAS spectra show the expected strong polarization dependence, due to the directionality of the C 2p orbitals (Hemraj-Benny *et al.*, 2006). Absorption into the π^* orbitals dominates when the light polarization is predominantly out of the graphitic sp^2 carbon planes (polarization angle close to 0, corresponding to horizontal polarization), while the σ^* resonances prevail when the light polarization is parallel to the graphite carbon planes (polarization angles close to +90°, corresponding to vertical polarization with positive undulator phase, or −90°, corresponding to vertical polarization with negative phase).
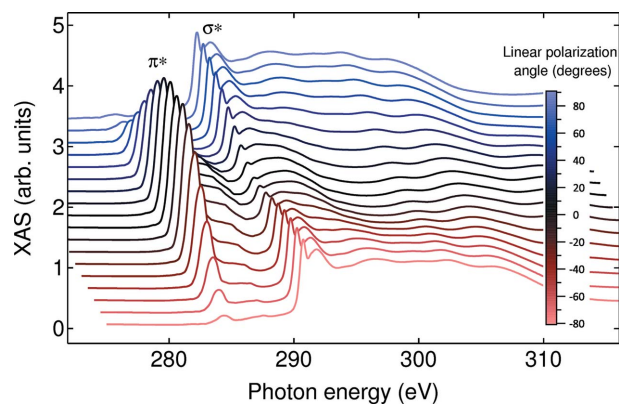

Figure 3
Polarization-dependent XAS of a HOPG crystal measured at the C K-edge. The spectra are offset both horizontally and vertically for clarity.
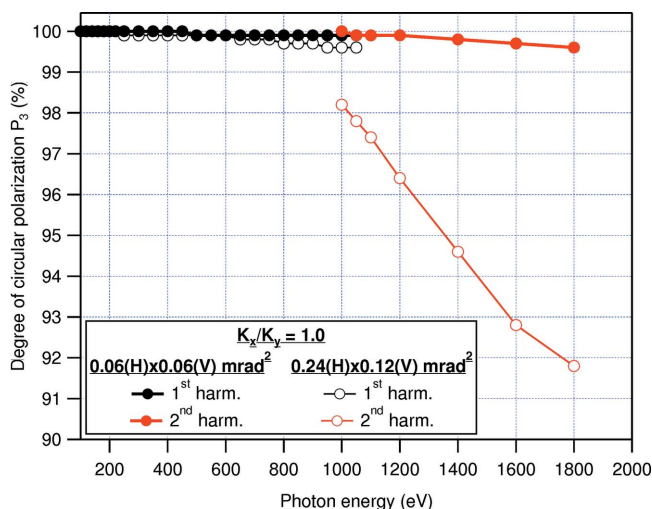
Figure 4
Photon energy and undulator harmonic dependence of the degree of circular polarization calculated for two extreme values of the beamline angular acceptance, in the energy range 100–2000 eV.

Figure 5
Normalized photon flux as a function of the ratio K_x/K_y at selected energies of (*a*) 1200 eV and (*b*) 3000 eV, for an angular acceptance of 0.24 mrad × 0.12 mrad.

3.1.2. Circular and elliptical polarization. The degree of circular polarization emitted by the Apple-II undulator, defined as the ratio $P_3 = S_3/S_0$ of the Stokes parameters S_3 and S_0, is related to the parameters K_x and K_y, which are proportional to the two perpendicular components of the magnetic field of the undulator (Clarke, 2004). For a given ratio K_x/K_y, P_3 depends both on the photon energy and on the undulator harmonic. For energies up to about 1000 eV, the beamline is operated in the first harmonic with $K_x/K_y = 1$, giving fully circularly polarized radiation. Taking into account the finite angular acceptance of the beamline and the finite emittance of the electron beam, the degree of circular polarization calculated with *ART* is above 99.6% at all energies up to 1050 eV when the full undulator beam is accepted, *i.e.* integrating in an angular range of 0.24 mrad × 0.12 mrad (horizontal × vertical), as shown in Fig. 4. P_3 is above 99.9% with a reduced angular acceptance of 0.06 mrad × 0.06 mrad. Calculations including the measured magnetic field profile of the undulator, performed using the code *SPECTRA* (Tanaka & Kitamura, 2001), confirm that the degree of circular polarization at the sample is of the order of at least 98% for a beamline angular acceptance of 0.24 mrad × 0.12 mrad, while it is above 99.5% for angular apertures below 0.12 mrad × 0.12 mrad.

Above 1000 eV, higher undulator harmonics are used, and the beamline control offers full flexibility in the choice of the harmonic and degree of circular polarization to be used for each experiment. The choice is between maximizing the degree of circular polarization at the expense of the photon flux (due to the intrinsic absence of on-axis emission for even harmonics and of on-axis emission of circular polarization for all harmonics above the first) or maximizing the flux at the expense of the purity of circular polarization. Fig. 5(*a*) shows the photon flux calculated using *ART* for an energy of 1200 eV for the second and third undulator harmonics as a function of the ratio K_x/K_y, at a beamline angular acceptance of
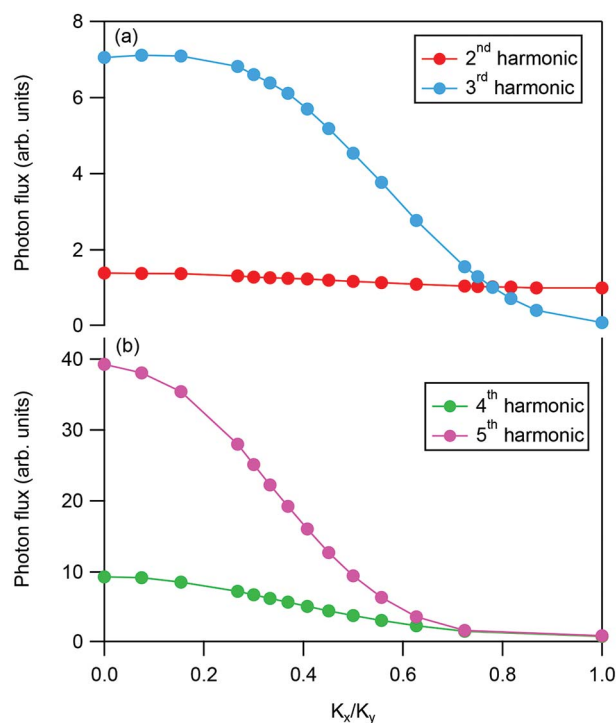
0.24 mrad × 0.12 mrad. The data shown are normalized to the flux in the second harmonic and $K_x/K_y = 1$. For $K_x/K_y \geq 0.8$ (*i.e.* for large P_3), the flux is higher in the second harmonic. However, for lower rates of circular polarization, the flux in the third harmonic becomes quickly higher than that of the second, while the latter shows little dependence on K_x/K_y. The beamline can therefore be operated in the second harmonic when a degree of circular polarization close to 100% is desired. In this case, Fig. 4 shows that P_3 is higher than 99.5% for energies up to 1800 eV with a reduced beamline acceptance of 0.06 mrad × 0.06 mrad. However, P_3 decays quickly with increasing energy at the nominal beamline acceptance of 0.24 mrad × 0.12 mrad. For this reason, in the energy range between 1000 and 2000 eV, it is generally more convenient to work with the third undulator harmonic and with $K_x < K_y$. For example, with $K_x/K_y = 0.63$, besides the increase of flux by a factor of almost three with respect to the second harmonic with $K_x/K_y = 1$ (see Fig. 5*a*), the degree of circular polarization P_3 is independent of the beamline angular acceptance and still high, in the range 95–97% as depicted in Fig. 6.

At energies above 2000 eV, the difference between even and odd harmonics is even more evident, as exemplified in Fig. 5(*b*) for the case of the fourth and fifth harmonics at a photon energy of 3000 eV. Here the odd harmonic has higher flux than the preceding even one for any value of K_x/K_y. The beamline is therefore operated with odd harmonics in this energy range, with a ratio $K_x/K_y = 0.4$ delivering a rate of circular polarization in the range 75–85%, depending on photon energy, as shown in Fig. 7. It is worth noting that this
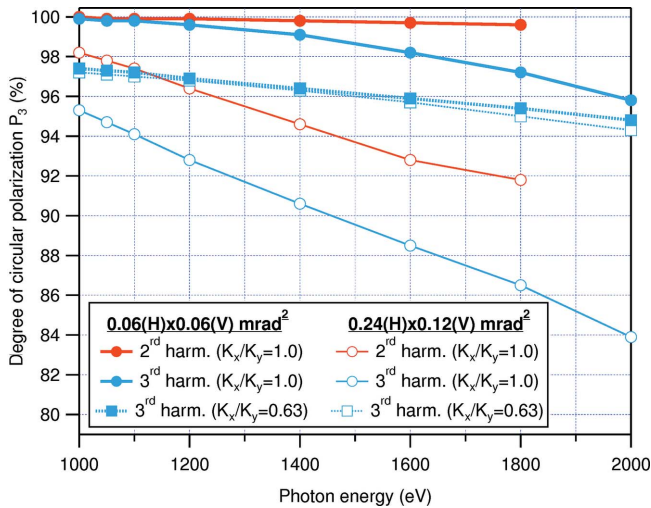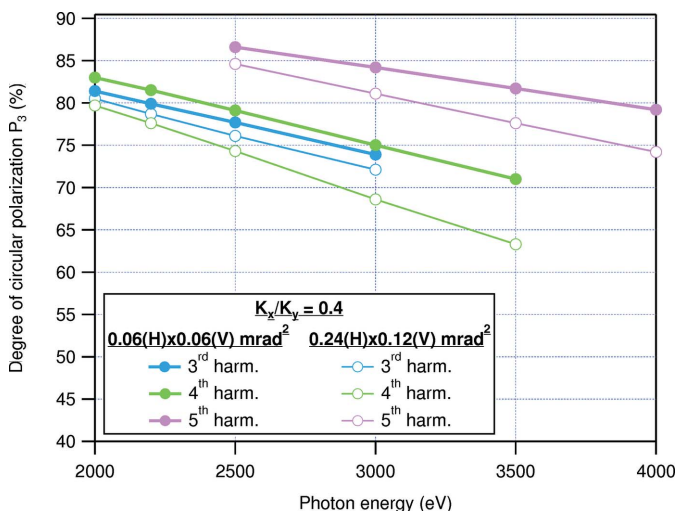
Figure 6
Comparison of the photon energy and undulator harmonic dependence of the degree of circular polarization calculated for two extreme values of the b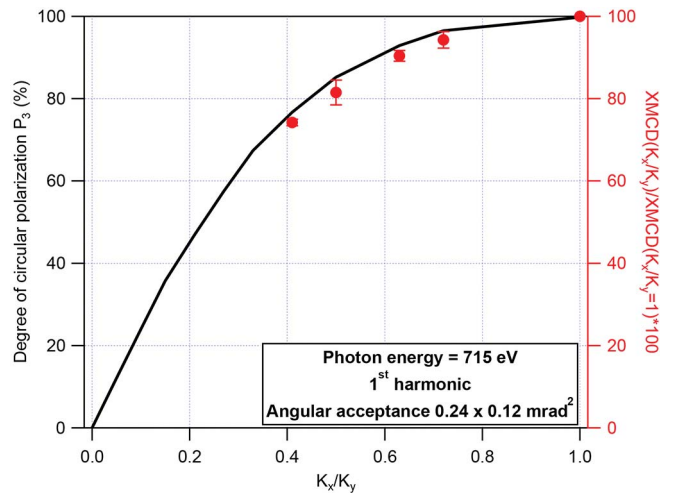eamline angular acceptance, in the energy range 1000–2000 eV, with second and third harmonics with $K_x/K_y = 1$ and with the third harmonic and $K_x/K_y = 0.63$.

Figure 8
K_x/K_y dependence of the calculated degree of circular polarization (continuous line, left axis) at 715 eV in first harmonic and of the XMCD recorded at the Fe $L_{2,3}$-edges on a metallic Fe film, normalized to its value for $K_x/K_y = 1$ (red circles, right axis).

low K_x/K_y mode of operation also minimizes the flux difference between linear and elliptical polarizations to a factor of two as compared with 40 in the case of $K_x/K_y = 1$.

Finally, Fig. 8 depicts the K_x/K_y dependence of the calculated degree of circular polarization emitted by the undulator in its first harmonic at a photon energy of 715 eV and the corresponding dependence of the XMCD recorded at the Fe $L_{2,3}$-edges (normalized to its value at $K_x/K_y = 1$) on a film of metallic Fe. The good agreement between experiment and calculation confirms the correct operation of the undulator and its control system.

3.2. Flux at the sample

The flux delivered by the beamline at the sample position was measured with a Si photodiode for all photon beam

polarizations and combinations of plane gratings and spherical mirrors, by using the Au-coated stripe of PM, and with ES and XS openings fixed to 15 μm, corresponding to the standard working conditions of the beamline.

Fig. 9(a) displays the photon flux measured at the sample position (full symbols) with a beamline angular acceptance of 0.24 mrad × 0.12 mrad, for linear polarization, normalized to

Figure 7
Photon energy and undulator harmonic dependence of the degree of circular polarization calculated for two extreme values of the beamline angular acceptance, in the energy range 2000–4000 eV.
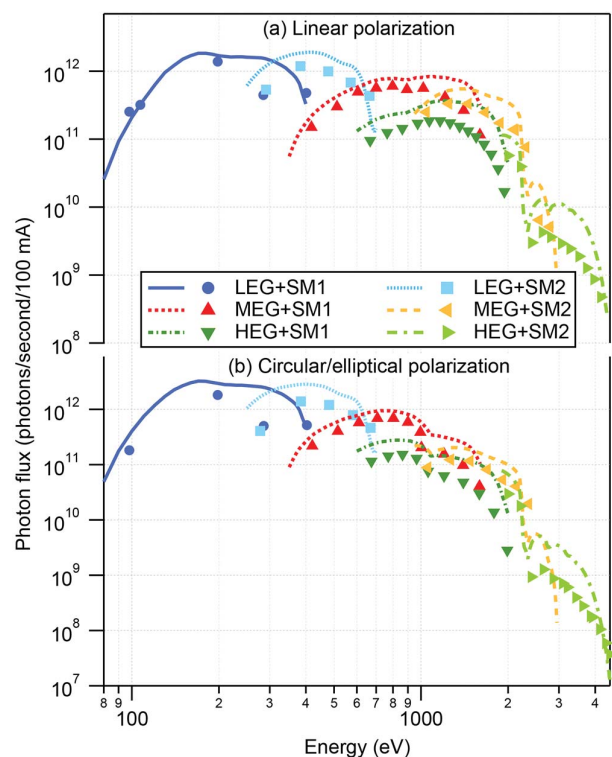

Figure 9
Measured (symbols) and calculated (lines) flux at the sample, with ES and XS opening of 15 μm and 100 mA electron beam current, for (a) linear polarization and (b) circular (up to 1100 eV) or elliptical (above 1100 eV) polarization.

100 mA electron beam current and compares it with the flux calculated under the same conditions by ray tracing (lines) using *ART*, including the gratings diffraction efficiency as calculated by *REFLEC* and *ART*. The first harmonic of the undulator was used for energies up to 900 eV, above which higher (odd) harmonics up to the seventh were used. Fig. 9(*b*) shows the same comparison for circular (up to a photon energy of 1100 eV) or elliptical (above 1100 eV) polarizations. In the case of elliptical polarization (*i.e.* at photon energies above 1100 eV), we used K_x/K_y = 0.63 up to 2400 eV and K_x/K_y = 0.4 at higher energies.

For all combinations of gratings and spherical mirrors and for all polarizations the measured flux perfectly follows the calculated energy dependence. However, it is systematically lower than what is expected from calculations, typically by a factor of less than two, but increasing at higher energies. There are a number of factors that contribute to this, which are not accounted for in the simulation. Among them, the most significant ones are the actual density of reflective coatings, carbon contamination on mirror and grating coatings, small misalignments and phase errors of the source.

3.3. Energy resolution

The energy resolution of the beamline was determined by recording the absorption of gases in a gas cell permanently installed at the beamline downstream of the monochromator exit slit, at a gas pressure of about 6×10^{-6} mbar. This was done at three photon energies corresponding to the $L_{2,3}$-edges of gaseous Ar (around 245 eV) and to the K-edges of gaseous N_2 and Ne (around 400 and 870 eV, respectively), thus effectively allowing for the resolution of each grating to be determined for at least one energy. The shape of the gas absorption peaks can be described by Voigt functions, which consist of the convolution of a Lorentzian function describing the finite life-time of the core hole as well as the vibrational broadening, and a Gaussian function describing the photon energy bandwidth of the monochromator. This method is generally reliable when the energy resolution to be determined is of the same order of magnitude as the natural width of the measured core-level transition, corresponding to resolving powers not exceeding ~10000.

Fig. 10 shows the Ar $2p_{3/2} \rightarrow 4s$ absorption line, measured with the LEG + SM1 combination with ES and XS opening of 15 μm, together with the fitted Voigt profile. This yields a Lorentzian FWHM of 112 (3) meV, in agreement with previous reports (Zangrando *et al.*, 2004; Belkhou *et al.*, 2015), and a Gaussian FWHM of 34 (3) meV, corresponding to a resolving power $E/\Delta E \simeq 7000$.

Fig. 11 shows the N_2 $1s \rightarrow \pi^*$ absorption spectrum, measured with the LEG + SM2 combination with XS opening of 5 μm. Seven absorption lines are resolved and the spectrum is thus fitted with a superposition of seven Voigt profiles. This yields a Lorentzian FWHM of 114 (2) meV, in agreement with previous reports (Strocov *et al.*, 2010; Piamonteze *et al.*, 2012; Yamamoto *et al.*, 2014; Belkhou *et al.*, 2015), and a Gaussian FWHM of 26 (2) meV, corresponding to a resolving power
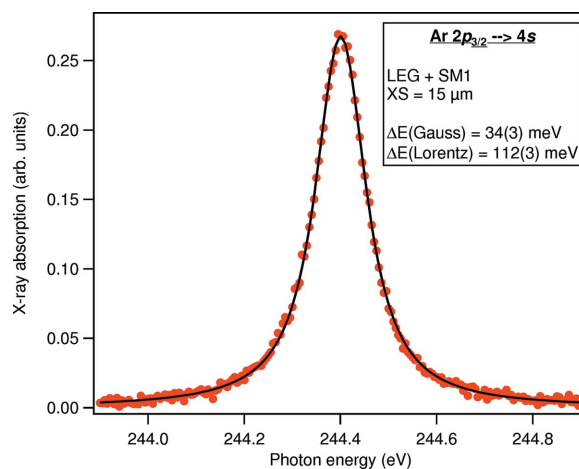
Figure 10
Ar gas $2p_{3/2} \rightarrow 4s$ transition measured with SM1 + LEG (symbols) and corresponding fit with a Voigt profile (line).

$E/\Delta E \simeq 15000$. An alternative method, independent of the uncertainty in the value of the Lorentzian width of the N_2 $1s$ absorption lines, is based on the intensity ratio between the first valley and the third peak of the N_2 $1s \rightarrow \pi^*$ spectra (Chen & Sette, 1989), which is low (*i.e.* well below a value of 1) at high energy resolving power, leading to highly resolved spectroscopic features. We find a value of 0.66 in the spectrum of Fig. 11, compatible with the values reported by Follath *et al.* (2004), Piamonteze *et al.* (2012) and Belkhou *et al.* (2015), which have been associated with a resolving power above 10000, in agreement with the Voigt fitting. For an XS opening of 15 μm, corresponding to the standard working conditions of the beamline, we find a Gaussian FWHM of 67 (2) meV, corresponding to a resolving power $E/\Delta E \simeq 6000$.

Fig. 12(*a*) shows the Ne $1s \rightarrow 3p$ absorption spectrum, measured with the MEG + SM1 combination with XS opening of 5 μm. The energy resolution is obtained by fitting the measured line profile with a single Voigt curve, with a fixed Lorentzian width of 245 meV, an average of the lowest values for the width of the Ne $1s$ absorption line used in the recent
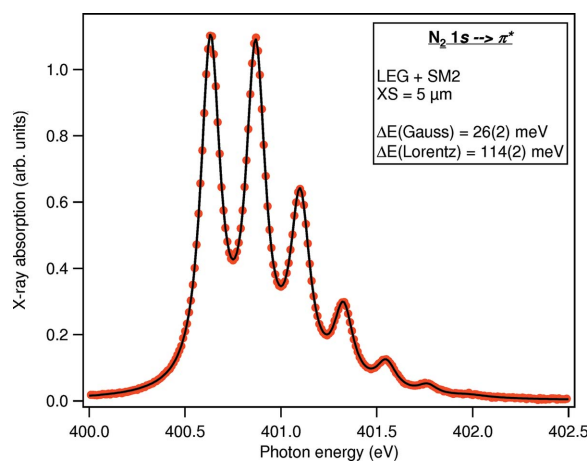
Figure 11
N_2 gas $1s \rightarrow \pi^*$ transition measured with SM2 + LEG (symbols) and corresponding fit with the superposition of seven Voigt lines (line).
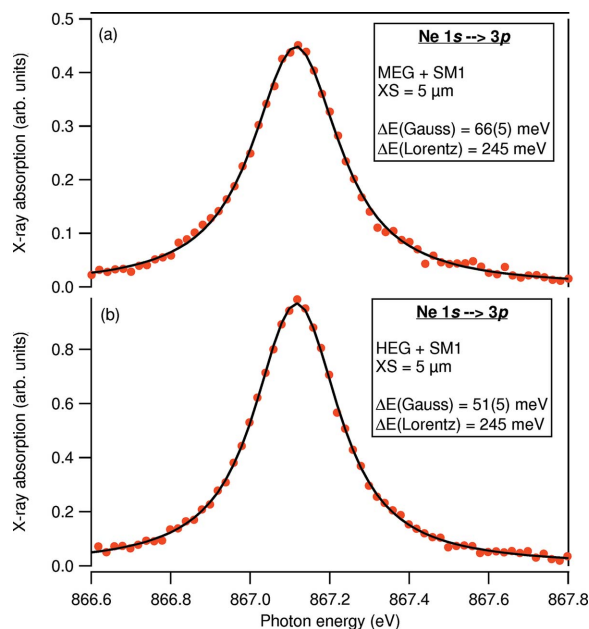
Figure 12
Ne gas $1s \rightarrow 3p$ transition measured (symbols) with (a) SM1 + MEG and (b) SM1 + HEG, and corresponding fits with a Voigt profile (lines).

Figure 13
Comparison between measured (symbols) and calculated (lines) energy resolving power for an exit slit opening of (a) 5 µm and (b) 15 µm.

literature (Strocov *et al.*, 2010; Piamonteze *et al.*, 2012; Yamamoto *et al.*, 2014; Belkhou *et al.*, 2015; Ohresser *et al.*, 2014). The fit yields an energy resolution of $\Delta E = 66\ (5)$ meV, corresponding to a resolving power of $E/\Delta E \simeq 13000$, which reduces to ∼7000 with the standard openings of the XS of 15 µm. In Fig. 12(b) the Ne $1s \rightarrow 3p$ absorption spectrum, measured with the HEG + SM1 combination with XS openings of 5 µm, is shown. The extracted energy resolution is 51 (5) meV, corresponding to a resolving power $E/\Delta E \simeq 17000$. The latter goes down to ∼10000 under the standard working conditions of the beamline, with an XS opening of 15 µm.

The final comparison between the measured energy resolution and that calculated by the ray-tracing for XS openings of 5 and 15 µm are shown in Figs. 13(a) and 13(b), respectively, for all combinations of gratings and spherical mirrors and by taking into account the actual measured figure errors of all involved optical elements. There is an excellent agreement between theory and experiment, with resolving powers between 5000 and 10000 for an XS opening of 15 µm and in excess of 10000 at 5 µm XS opening. The only notable discrepancy is found for the LEG + SM2 combination at the Ar $2p_{3/2} \rightarrow 4s$ transition (corresponding to the low-energy extreme of this grating/mirror combination) where the measured resolution is considerably lower than the corresponding calculation. For the low-energy end of a grating, the beam footprint exceeds the geometrical acceptance of the grating, and this induces photon beam diffraction (not included in the ray tracing) which results in being the limiting factor of the monochromatic spot size at the exit slit plane. A further contribution in limiting the energy resolution can be small fabrication errors in the D_1 and especially D_2 parameters of the grating, which have an amplified effect at the low-energy extreme of its working range.
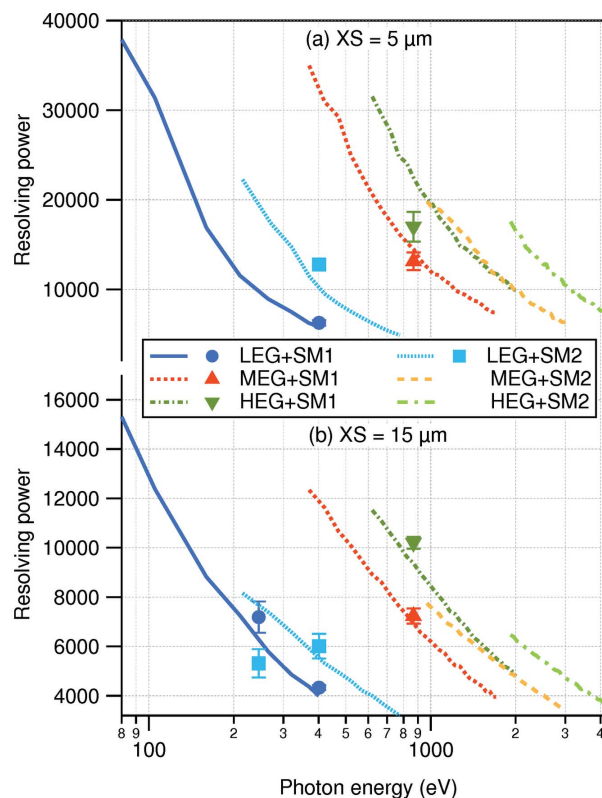
Due to the impossibility of determining experimentally the energy resolution through the absorption of gases, we assessed the performance of the BOREAS monochromator at energies above 2000 eV by recording absorption spectra of various solids. We present here two examples testifying the high quality of the XAS spectra that can be recorded in this energy range. Fig. 14(a) shows the S K-edge spectrum recorded on a soil specimen of $CaSO_4 \cdot 2H_2O$, while panel (b) of the same figure depicts the Ru $L_{2,3}$ XAS of a $SrRuO_3$ thin film. All spectral features are well resolved, as by comparison with previously reported measurements performed with double-crystal monochromators (Fleet, 2005; Liu *et al.*, 2013). The results of the first X-ray magnetic circular dichroism experiment at the Ru $L_{2,3}$-edges have already been published (Agrestini *et al.*, 2015).

3.4. Reproducibility of the photon energy scale

For XMCD experiments, which are based on the subtraction of pairs of X-ray absorption spectra recorded in sequence, the reproducibility of the energy scale of the monochromator in successive scans is an important parameter. Ideally, this should be a small fraction of the energy resolution, which in typical experiments is of the order of 100–200 meV. We have verified the reproducibility of the BOREAS monochromator by recording 120 successive XAS scans across the Ti $L_{2,3}$-edges on a thin film of TiO_2. Each energy scan has a duration of about 2 min, thus the test spans a time frame of more than
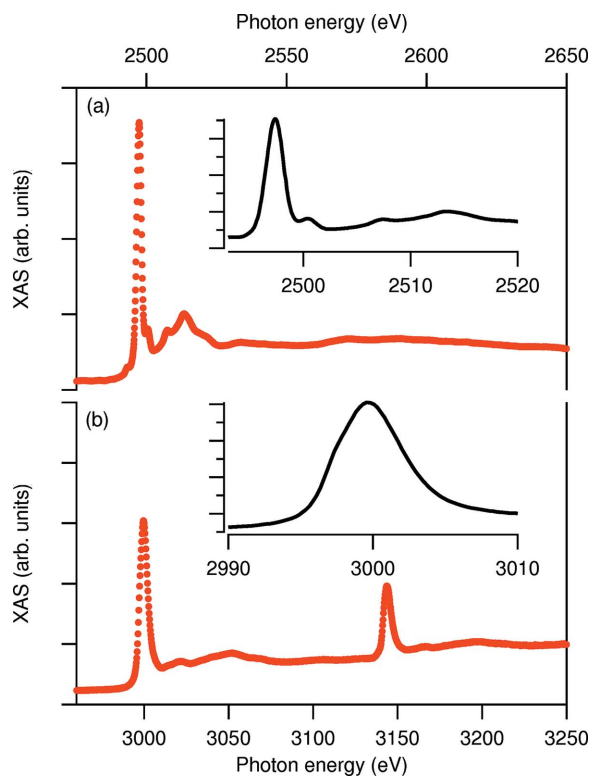
Figure 14
XAS of (*a*) CaSO$_4$·2H$_2$O at the sulfur *K*-edge and of (*b*) SrRuO$_3$ at the ruthenium $L_{2,3}$-edges. The insets show the detail of the most prominent features of the corresponding spectra.

Figure 15
Dependence of the energy of the main peak of the Ti L_3-edge of a TiO$_2$ thin film from scan number, before (black squares) and after (red circles) correction with a reference sample. The inset shows the full Ti $L_{2,3}$-edges XAS scan, with its main peak indicated by an arrow.

4 h. Fig. 15 shows, as black squares, the energy (relative to its value averaged over all scans) of the sharpest peak at the Ti L_3-edge (indicated by an arrow in the inset of the figure) as a function of scan number. The maximum deviations from the average value of the energy are of less than ±10 meV, *i.e.* a factor of about ten lower than the typical energy resolution, with a standard deviation of about 5 meV. The reproducibility can be further greatly enhanced by recording simultaneously the XAS of a reference polycristalline TiO$_2$ sample placed on the tail of the X-ray beam (thus typically attenuating by only about 1% the intensity of the beam on the main sample). In fact, by rescaling the energy with such a reference, the reproducibility is improved by a factor of ten, as shown by the red circles in Fig. 15. For this reason, BOREAS is equipped with a dedicated chamber, located far from any stray magnetic field, equipped with a standard set of non-magnetic and polycristalline reference samples covering the main absorption edges and with free space for more user-specified reference samples.

4. Concluding remarks

We have discussed the optical design of the BOREAS beamline at the ALBA synchrotron radiation facility. It was optimized for XMCD and RSXS experiments in the unusually extended energy range 80–4500 eV, entirely covered with a grating monochromator. The results of the commissioning, i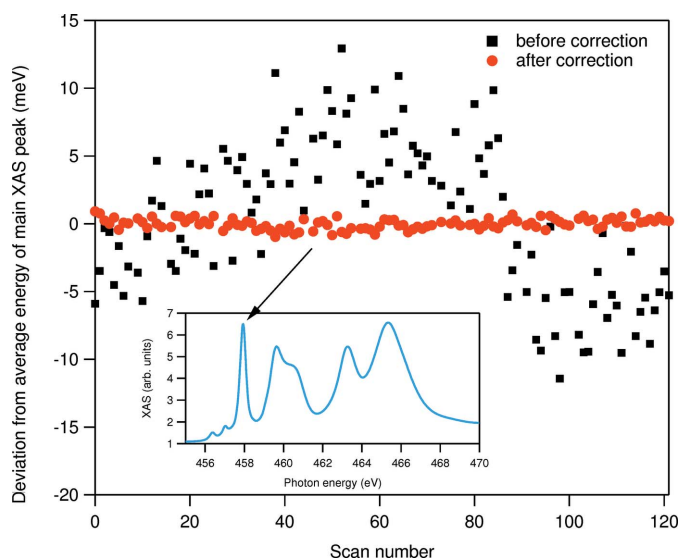n agreement with ray-tracing simulations, show the excellent performance of the beamline in terms of both photon flux and energy resolution and reproducibility.

References

Agrestini, S., Hu, Z., Kuo, C.-Y., Haverkort, M. W., Ko, K.-T., Hollmann, N., Liu, Q., Pellegrin, E., Valvidares, M., Herrero-Martin, J., Gargiani, P., Gegenwart, P., Schneider, M., Esser, S., Tanaka, A., Komarek, A. C. & Tjeng, L. H. (2015). *Phys. Rev. B*, **91**, 075127.
Beaurepaire, E., Bulou, H., Joly, L. & Scheurer, F. (2013). Editors. *Magnetism and Synchrotron Radiation: Towards the Fourth Generation Light Sources*, Vol. 151 of *Springer Proceedings in Physics*. Springer International Publishing.
Belkhou, R., Stanescu, S., Swaraj, S., Besson, A., Ledoux, M., Hajlaoui, M. & Dalle, D. (2015). *J. Synchrotron Rad.* **22**, 968–979.
Campmany, J., Marcos, J., Massana, V., Becheri, F., Gigante, J. V., Colldelram, C. & Ribó, L. (2013). *J. Phys. Conf. Ser.* **425**, 032010.
Carbone, C., Gardonio, S., Moras, P., Lounis, S., Heide, M., Bihlmayer, G., Atodiresei, N., Dederichs, P. H., Blügel, S., Vlaic, S., Lehnert, A., Ouazi, S., Rusponi, S., Brune, H., Honolka, J., Enders, A., Kern, K., Stepanow, S., Krull, C., Balashov, T., Mugarza, A. & Gambardella, P. (2011). *Adv. Funct. Mater.* **21**, 1212–1228.
Chen, C. T. & Sette, F. (1989). *Rev. Sci. Instrum.* **60**, 1616–1621.
Clarke, J. A. (2004). *The Science and Technology of Undulators and Wigglers.* Oxford University Press.
Einfeld, D. (2011). *Proceedings of the 2nd International Conference on Particle Accelerators (IPAC 2011)*, San Sebastian, Spain, 4–9 September 2011, Vol. C110904.

Fleet, M. E. (2005). *Can. Mineral.* **43**, 1811–1838.

Follath, R. (2001). *Nucl. Instrum. Methods. Phys. Res. A*, **467–468**, 418–425.

Follath, R. (2004). *AIP Conf. Proc.* **705**, 348–351.

Follath, R. & Senf, F. (1997). *Nucl. Instrum. Methods Phys. Res. A*, **390**, 388–394.

Hemraj-Benny, T., Banerjee, S., Sambasivan, S., Balasubramanian, M., Fischer, D. A., Eres, G., Puretzky, A. A., Geohegan, D. B., Lowndes, D. H., Han, W., Misewich, J. A. & Wong, S. S. (2006). *Small*, **2**, 26–35.

Hettrick, M. C. & Underwood, J. H. (1986). *Appl. Opt.* **25**, 4228–4231.

Kirkpatrick, P. & Baez, A. V. (1948). *J. Opt. Soc. Am.* **38**, 766–774.

Liu, H.-J., Tra, V.-T., Chen, Y.-J., Huang, R., Duan, C.-G., Hsieh, Y.-H., Lin, H.-J., Lin, J.-Y., Chen, C.-T., Ikuhara, Y. & Chu, Y.-H. (2013). *Adv. Mater.* **25**, 4753–4759.

Nicolás, J., Barla, A. & Juanhuix, J. (2013). In *Proc. SPIE*, **8848**, 88480Z.

Ohresser, P., Otero, E., Choueikani, F., Chen, K., Stanescu, S., Deschamps, F., Moreno, T., Polack, F., Lagarde, B., Daguerre, J.-P., Marteau, F., Scheurer, F., Joly, L., Kappler, J.-P., Muller, B., Bunau, O. & Sainctavit, P. (2014). *Rev. Sci. Instrum.* **85**, 013106.

Piamonteze, C., Flechsig, U., Rusponi, S., Dreiser, J., Heidler, J., Schmidt, M., Wetter, R., Calvi, M., Schmidt, T., Pruchova, H., Krempasky, J., Quitmann, C., Brune, H. & Nolting, F. (2012). *J. Synchrotron Rad.* **19**, 661–674.

Rogalev, A., Ollefs, K. & Wilhelm, F. (2016). *X-ray Absorption and X-ray Emission Spectroscopy*, edited by J. A. V. Bokhoven and C. Lamberti, pp. 671–694. New York: John Wiley and Sons.

Sasaki, S. (1994). *Nucl. Instrum. Methods. A*, **347**, 83–86.

Schäfers, F., Abramsohn, D. & Krumrey, M. (2002). *Reflec, a program to calculate VUV/X-ray optical elements and synchrotron radiation beamlines.* BESSY, Berlin, Germany.

Stöhr, J. & Siegmann, H. C. (2006). *Magnetism – From Fundamentals to Nanoscale Dynamics*, Vol. 152 of *Springer Series in Solid-State Sciences.* Berlin Heidelberg: Springer-Verlag.

Strocov, V. N., Schmitt, T., Flechsig, U., Schmidt, T., Imhof, A., Chen, Q., Raabe, J., Betemps, R., Zimoch, D., Krempasky, J., Wang, X., Grioni, M., Piazzalunga, A. & Patthey, L. (2010). *J. Synchrotron Rad.* **17**, 631–643.

Tanaka, T. & Kitamura, H. (2001). *J. Synchrotron Rad.* **8**, 1221–1228.

Underwood, J. H. & Koch, J. A. (1997). *Appl. Opt.* **36**, 4913–4921.

Yamamoto, S., Senba, Y., Tanaka, T., Ohashi, H., Hirono, T., Kimura, H., Fujisawa, M., Miyawaki, J., Harasawa, A., Seike, T., Takahashi, S., Nariyama, N., Matsushita, T., Takeuchi, M., Ohata, T., Furukawa, Y., Takeshita, K., Goto, S., Harada, Y., Shin, S., Kitamura, H., Kakizaki, A., Oshima, M. & Matsuda, I. (2014). *J. Synchrotron Rad.* **21**, 352–365.

Zangrando, M., Zacchigna, M., Finazzi, M., Cocco, D., Rochow, R. & Parmigiani, F. (2004). *Rev. Sci. Instrum.* **75**, 31–36.